 CMES, vol.10, no.1, pp.79-95, 2005

Non-uniform Hardening Constitutive Model for Compressible Orthotropic Materials with Application to Sandwich Plate Cores

Zhenyu Xue[1], **Ashkan Vaziri**[1] **and John W. Hutchinson**[1]

Abstract: A constitutive model for the elastic-plastic behavior of plastically compressible orthotropic materials is proposed based on an ellipsoidal yield surface with evolving ellipticity to accommodate non-uniform hardening or softening associated with stressing in different directions. The model incorporates rate-dependence arising from material rate-dependence and micro-inertial effects. The basic inputs are the stress-strain responses under the six fundamental stress histories in the orthotropic axes. Special limits of the model include classical isotropic hardening theory, the Hill model for incompressible orthotropic solids, and the Deshpande-Fleck model for highly porous isotropic foam metals. A primary motivation is application to metal core structure in sandwich plates wherein the core is modeled by a continuum constitutive model. The constitutive model is implemented within a finite element framework to represent the behavior of square honeycomb metal cores of sandwich plates subject to quasi-static and dynamic loads. Input identification is illustrated for numerical formulations that employ one element through the core thickness. Representations of the core with one element through the thickness are shown to be able to capture most of the important influences of nonlinear core behavior on overall response of sandwich plates under both quasi-static and dynamic loadings.

keyword: Constitutive model, plasticity, rate-dependence, homogenization, sandwich plate, square honeycombs.

1 Introduction

A primary motivation of the work in this paper is the development of a constitutive representation of core structure for metal sandwich plates that will allow efficient numerical solution of large structural problems under a wide range of static and dynamic loads. The starting point is the formulation of a continuum model for a general class of plastically compressible, orthotropic solids based on an ellipsoidal yield surface which incorporates non-uniform hardening. The constitutive model has considerable flexibility. Limits of the model include many of the important phenomenological constitutive relations for elastic-plastic solids: classical isotropic plasticity, Hill's theory for incompressible orthotropic plasticity, and the Deshpande-Fleck theory for highly compressible isotropic metal foams. A salient feature of the formulation is its ability to model distinct hardening or softening behaviors under different stressing conditions, with application to both plastically incompressible solids and highly compressible materials.

For application to metal sandwich cores, the approach requires inputs specifying the stress-strain behavior characterizing single component stressing in orthotropic axes for each of the six components of stress. These basic inputs can be obtained from theoretical models, experimental data or numerical simulations, or combinations of all three. Once the inputs are characterized, the constitutive model can be used to represent the core in connection with standard finite element codes. In this paper, the commercial code ABAQUS Explicit has been used in connection with a user-supplied subroutine that has been constructed based on the constitutive model. The paper illustrates the process of identifying the input stress-strain data for square honeycomb cores. It also demonstrates that representing the core by elements extending all the way through the core can be accurate and highly efficient in the analysis of sandwich plates deformed under quasi-static and dynamic loads to large deflections. Simulations based on full three-dimensional meshing of the core demonstrate the validity of the approach.

The present paper continues the effort underway for several years by a number of groups to develop continuum constitutive relations to characterize a range of core structures and to validate them for structural applications [Deshpande, Fleck and Ashby (2001); Hanssen, Langseth and Hopperstad (2002); Mohr and Doyoyo

[1] Harvard University, Cambridge, MA, U.S.A

(2004); Oller, Car and Lubliner (2003); Qiu, Deshpande and Fleck (2003); Rabczuk, Kim, Samaniego and Belytschko (2004); Xue and Hutchinson (2003; 2004a; 2005); Zok, Rathbun, He, Ferri, Mercer, McMeeking and Evans (2005)]. Parallel efforts have been made to compare experimental observations on statically and dynamically loaded sandwich plates with theoretical and numerical simulations [Cote, Deshpande, Fleck and Evans (2004); Dharmasena, Xue, Wadley and Hutchinson (2005); Rathbun, Radford, Xue, He, Yang, Deshpande, Fleck, Hutchinson, Zok and Evans (2005)]. This paper extends the constitutive model proposed in earlier papers by Xue and Hutchinson [2004a; 2005] by including both non-uniform hardening and a more general representation of transverse strains. In addition, the present paper focuses on numerical approaches that employ meshes with only one element through the thickness of the core—a decision that has important implications in the process of identifying the constitutive inputs in dynamic applications. The present paper complements earlier work of [Rabczuk, Kim, Samaniego and Belytschko (2004)] who demonstrated that folded plate cores could be accurately represented without meshing through the core thickness using a direct homogenization approach that bypasses the introduction of a continuum constitutive model.

2 A continuum model for elastic-plastic behavior of plastically compressible orthotropic materials with non-uniform hardening or softening evolution

In this section, a constitutive model is prescribed for the elastic-plastic response of orthotropic materials under multi-axial stressing. The model allows hardening or softening behavior that can differ for stressing in each of the six fundamental stressing histories in orthotropic axes. Strain rate sensitivity is also taken into account.

2.1 Ellipsoidal yield surface and associated plastic flow rule

An ellipsoidal yield surface is proposed for plastically compressible metallic materials with microstructures including, among others, foams, lattice materials with truss elements, and honeycombs with plate elements. The constitutive model generalizes Hill's model for plastically incompressible orthotropic materials by incorporating both compressibility and evolving ellipticity of the yield surface reflecting differential hardening or softening in different stressing directions. The model extends earlier versions [Xue and Hutchinson (2004a; 2005)], as described below.

Let the x_i axes be aligned with the orthotropic axes of the material. Introduce stress, strain and plastic strain vectors in the usual way with

$$\begin{aligned}
\sigma &= (\sigma_1,\sigma_2,\sigma_3,\sigma_4,\sigma_5,\sigma_6)^T \\
&\equiv (\sigma_{11},\sigma_{22},\sigma_{33},\sigma_{13},\sigma_{23},\sigma_{12}) \\
\varepsilon &= (\varepsilon_1,\varepsilon_2,\varepsilon_3,\varepsilon_4,\varepsilon_5,\varepsilon_6) \\
&\equiv (\varepsilon_{11},\varepsilon_{22},\varepsilon_{33},2\varepsilon_{13},2\varepsilon_{23},2\varepsilon_{12}) \\
\varepsilon^P &= (\varepsilon_1^P,\varepsilon_2^P,\varepsilon_3^P,\varepsilon_4^P,\varepsilon_5^P,\varepsilon_6^P) \\
&\equiv (\varepsilon_{11}^P,\varepsilon_{22}^P,\varepsilon_{33}^P,2\varepsilon_{13}^P,2\varepsilon_{23}^P,2\varepsilon_{12}^P)
\end{aligned} \tag{1}$$

The ellipsoidal yield surface for orthotropic materials can be written in the form

$$f \equiv \sigma_{eff} - \sigma_0 = 0 \tag{2}$$

where the effective stress σ_{eff} is defined by

$$\begin{aligned}
\left(\frac{\sigma_{eff}}{\sigma_0}\right)^2 &= \left(\frac{\sigma_1}{\tilde{\sigma}_1}\right)^2 + \left(\frac{\sigma_2}{\tilde{\sigma}_2}\right)^2 + \left(\frac{\sigma_3}{\tilde{\sigma}_3}\right)^2 \\
&+ \left(\frac{\sigma_4}{\tilde{\sigma}_4}\right)^2 + \left(\frac{\sigma_5}{\tilde{\sigma}_5}\right)^2 + \left(\frac{\sigma_6}{\tilde{\sigma}_6}\right)^2 \\
&- 2\hat{\nu}_1\left(\frac{\sigma_2}{\tilde{\sigma}_2}\frac{\sigma_3}{\tilde{\sigma}_3}\right) - 2\hat{\nu}_2\left(\frac{\sigma_3}{\tilde{\sigma}_3}\frac{\sigma_1}{\tilde{\sigma}_1}\right) - 2\hat{\nu}_3\left(\frac{\sigma_1}{\tilde{\sigma}_1}\frac{\sigma_2}{\tilde{\sigma}_2}\right)
\end{aligned} \tag{3}$$

The stress quantity σ_0 is a *fixed* reference stress that can be chosen arbitrarily; it is simply a scaling factor. The coefficients, $\hat{\nu}_1$, $\hat{\nu}_2$ and $\hat{\nu}_3$, are directly related to plastic Poisson's ratios, as will be detailed later. They can be chosen to model incompressible materials, including Hill's anisotropic model, and they can be chosen to model highly compressible materials. In the most general case, these coefficients will vary as the deformation proceeds.

The basic inputs to the model are the six rate-dependent stress-strain curves, $\hat{\sigma}_i(\varepsilon_i^P,\dot{\varepsilon}_i^P)$, that characterize the plastic response of the continuum material under conditions when each of the above six (positive) stress components acts singly, together with the three $\hat{\nu}_i$. More precisely, when σ_i is the only non-zero stress component, let

$\hat{\sigma}_i(\varepsilon_i^P, \dot{\varepsilon}_i^P)$ denote the hardening (or softening) function specifying the dependence of σ_i on the associated plastic strain component, ε_i^P, when the strain-rate, $\dot{\varepsilon}_i^P$, is positive and constant. Thus, $\hat{\sigma}_1(\varepsilon_1^P, \dot{\varepsilon}_1^P)$ denotes stress-strain data for monotonic tensile stressing in the 1-direction, while $\hat{\sigma}_4(\varepsilon_4^P, \dot{\varepsilon}_4^P)$ is reserved for a pure shear stress in the (1,3) axes, etc. Once the strain and strain-rate dependence of the six functions, $\hat{\sigma}_i(\varepsilon_i^P, \dot{\varepsilon}_i^P)$, along with that of the three coefficients, $\hat{\nu}_i$, is specified in terms of the overall plastic strain and its rate, the yield surface is fully prescribed.

An associated plastic flow rule is adopted such that the plastic strain-rate is normal to the yield surface according to

$$\dot{\varepsilon}_i^P = \dot{\lambda}\frac{\partial f}{\partial \sigma_i} \tag{4}$$

where $\dot{\lambda}$ is the plastic strain-rate multiplier. Standard rules for plastic loading and elastic unloading apply. An effective plastic strain rate $\dot{\varepsilon}_{eff}^P$ is defined such that it is conjugate to the effective stress σ_{eff} through the plastic work rate:

$$\dot{W}^P = \sigma_i \dot{\varepsilon}_i^P = \sigma_{eff}\dot{\varepsilon}_{eff}^P \tag{5}$$

Because σ_{eff} is a homogeneous function of degree one of the stress, $\left(\sigma_i/\sigma_{eff}\right)\left(\partial\sigma_{eff}/\partial\sigma_i\right) \equiv 1$, and the relation $\dot{\varepsilon}_{eff}^P = \dot{\lambda}$ can be obtained in a straightforward manner by substituting (4) into (5). The flow rule (4) can be re-expressed as

$$\dot{\varepsilon}_i^P = \dot{\varepsilon}_{eff}^P\frac{\partial f}{\partial \sigma_i} \tag{6}$$

To make (6) more explicit and to obtain the expression for the effective plastic strain, rewrite the effective stress σ_{eff} in the matrix/vector form as

$$\sigma_{eff} = \left(\sigma \mathbf{P} \sigma\right)^{1/2} \tag{7}$$

where, from (3),

$$\mathbf{P} = \begin{bmatrix} \left(\frac{\sigma_0}{\hat{\sigma}_1}\right)^2 & -\frac{\hat{\nu}_3\sigma_0^2}{\hat{\sigma}_1\hat{\sigma}_2} & -\frac{\hat{\nu}_2\sigma_0^2}{\hat{\sigma}_3\hat{\sigma}_1} & 0 & 0 & 0 \\ -\frac{\hat{\nu}_3\sigma_0^2}{\hat{\sigma}_1\hat{\sigma}_2} & \left(\frac{\sigma_0}{\hat{\sigma}_2}\right)^2 & -\frac{\hat{\nu}_1\sigma_0^2}{\hat{\sigma}_2\hat{\sigma}_3} & 0 & 0 & 0 \\ -\frac{\hat{\nu}_2\sigma_0^2}{\hat{\sigma}_3\hat{\sigma}_1} & -\frac{\hat{\nu}_1\sigma_0^2}{\hat{\sigma}_2\hat{\sigma}_3} & \left(\frac{\sigma_0}{\hat{\sigma}_3}\right)^2 & 0 & 0 & 0 \\ 0 & 0 & 0 & \left(\frac{\sigma_0}{\hat{\sigma}_4}\right)^2 & 0 & 0 \\ 0 & 0 & 0 & 0 & \left(\frac{\sigma_0}{\hat{\sigma}_5}\right)^2 & 0 \\ 0 & 0 & 0 & 0 & 0 & \left(\frac{\sigma_0}{\hat{\sigma}_6}\right)^2 \end{bmatrix} \tag{8}$$

Then from (6),

$$\frac{\dot{\varepsilon}^P}{\dot{\varepsilon}_{eff}^P} = \frac{\mathbf{P}\sigma}{\sigma_{eff}} \tag{9}$$

Upon substituting this expression into (7) and simplifying, the effective plastic strain rate in terms of the strain rate components is[2]

$$\dot{\varepsilon}_{eff}^P = \left(\dot{\varepsilon}^{P\mathrm{T}}\mathbf{P}^{-1}\dot{\varepsilon}^P\right)^{1/2} \tag{10}$$

2.2 *Specification of* $\hat{\nu}_1$, $\hat{\nu}_2$ *and* $\hat{\nu}_3$ *using uniaxial stress histories*

For the each of the three basic uniaxial stress histories, define two instantaneous plastic "Poisson ratios" such that for uniaxial stressing in x_i direction, $\hat{\nu}_{ij}^P = -\dot{\varepsilon}_j^P \Big/ \dot{\varepsilon}_i^P$ $(j \neq i)$, which, in general, depend on ε_i^P. As a consequence of normality (9) and the assumed yield surface:

$$\begin{cases} \hat{\nu}_1 = \left(\frac{\hat{\sigma}_2}{\hat{\sigma}_3}\right)\hat{\nu}_{32}^P = \left(\frac{\hat{\sigma}_3}{\hat{\sigma}_2}\right)\hat{\nu}_{23}^P \\ \hat{\nu}_2 = \left(\frac{\hat{\sigma}_3}{\hat{\sigma}_1}\right)\hat{\nu}_{13}^P = \left(\frac{\hat{\sigma}_1}{\hat{\sigma}_3}\right)\hat{\nu}_{31}^P \\ \hat{\nu}_3 = \left(\frac{\hat{\sigma}_1}{\hat{\sigma}_2}\right)\hat{\nu}_{21}^P = \left(\frac{\hat{\sigma}_2}{\hat{\sigma}_1}\right)\hat{\nu}_{12}^P \end{cases} \tag{11}$$

providing the $\hat{\nu}_i$**,** along with three constraints on the six plastic Poisson ratios. Alternatively, if the $\hat{\nu}_i$ are specified, (11) gives the evolution of the plastic Poisson ratios

[2] $\mathbf{P}$ is singular in the limit when the material is plastically incompressible. The algorithm for solving the stresses in terms of the strain-rates described in the Appendix does not make use of the inverse of $\mathbf{P}$ and therefore the code developed applies whether or not the material is plastically incompressible.

as predicted by the constitutive model. Three possible choices for $\hat{\nu}_i$ are now noted to illustrate the generality of the formulation.

2.2.1 Zero plastic Poisson ratios

A particularly simple and useful choice is $\hat{\nu}_i = 0$ for $i = 1,3$, implying by (11) that the six plastic Poisson ratios vanish, as adopted earlier [Xue and Hutchinson (2005)]. Zero transverse straining is often a good approximation for low-density foams and lattice-type materials when subject to uniaxial stress because the members aligned perpendicular to the stress do not undergo significant strain. The off-diagonal terms in $\mathbf{P}$ vanish and the yield condition is then dependent only on the six inputs, $\hat{\sigma}_i(\varepsilon_i^P, \dot{\varepsilon}_i^P)$.

2.2.2 Isotropic foam model

The isotropic plasticity model for highly porous metal foams [Deshpande and Fleck (2000)] adopts an effective stress given by

$$\sigma_{eff}^2 = \left[1+\beta^2\right]^{-1}\left\{3s_{ij}s_{ij}/2+\beta^2\sigma_{kk}^2\right\} \tag{12}$$

Here,

$$s_{ij} = \sigma_{ij} - \frac{1}{3}\sigma_{kk}\delta_{ij}$$

and

$$\beta = \left[(1/2-\nu^P)/(1+\nu^P)\right]^{1/2}$$

where ν^P is the plastic Poisson's ratio under uniaxial stressing. The yield surface is a special case of the present yield surface (3) if

$$\begin{cases} \hat{\sigma}_1 = \hat{\sigma}_2 = \hat{\sigma}_3 = \sigma_0 \\ \hat{\sigma}_4 = \hat{\sigma}_5 = \hat{\sigma}_6 = \sigma_0\sqrt{3/(1+\beta^2)} \\ \hat{\nu}_1 = \hat{\nu}_2 = \hat{\nu}_3 = \nu^P \end{cases} \tag{13}$$

2.2.3 Hill's anisotropic plasticity model

Hill's yield surface [Hill (1947; 1950)] for plastically incompressible, orthotropic materials is obtained from (3) using normality to enforce $\dot{\varepsilon}_1^P + \dot{\varepsilon}_2^P + \dot{\varepsilon}_3^P \equiv 0$. This requirement is met if $\hat{\nu}_{12}^P + \hat{\nu}_{13}^P = 1$, $\hat{\nu}_{23}^P + \hat{\nu}_{21}^P = 1$ and $\hat{\nu}_{31}^P + \hat{\nu}_{32}^P = 1$, such that, by (11),

$$\begin{cases} \hat{\nu}_1 = \frac{1}{2}\left(\frac{\hat{\sigma}_2}{\hat{\sigma}_3} + \frac{\hat{\sigma}_3}{\hat{\sigma}_2} - \frac{\hat{\sigma}_2\hat{\sigma}_3}{\hat{\sigma}_1^2}\right) \\ \hat{\nu}_2 = \frac{1}{2}\left(\frac{\hat{\sigma}_3}{\hat{\sigma}_1} + \frac{\hat{\sigma}_1}{\hat{\sigma}_3} - \frac{\hat{\sigma}_1\hat{\sigma}_3}{\hat{\sigma}_2^2}\right) \\ \hat{\nu}_3 = \frac{1}{2}\left(\frac{\hat{\sigma}_1}{\hat{\sigma}_2} + \frac{\hat{\sigma}_2}{\hat{\sigma}_1} - \frac{\hat{\sigma}_1\hat{\sigma}_2}{\hat{\sigma}_3^2}\right) \end{cases} \tag{14}$$

Thus, the constitutive relation proposed here can model a plastically incompressible solid having six independent inputs $\hat{\sigma}_i(\varepsilon_i^P, \dot{\varepsilon}_i^P)$ characterizing single stress histories.

2.3 Independent hardening and coupled hardening

In the general case, for plastic loading with σ_i acting singly for either uniaxial or shear stressing in the axes of orthotropy:

$$\sigma_{eff}/\sigma_0 = |\sigma_i|/\hat{\sigma}_i \quad \text{(no summation on i)} \tag{15}$$

and, by (2), the current yield condition is $|\sigma_i| = \hat{\sigma}_i(\varepsilon_i^P, \dot{\varepsilon}_i^P)$. In particular, prior to any plastic deformation, the initial yield condition is $|\sigma_i| = \hat{\sigma}_i(0, \dot{\varepsilon}_i^P)$ when σ_i acts singly. Expressions for the effective plastic strain-rate from (10) can be determined in terms of the plastic strain components for each of the six basic stress histories. The direct calculation is tedious, but the outcome is simple and in accord with (5). For σ_i acting singly,

$$\dot{\varepsilon}_{eff}^P = \left|\dot{\varepsilon}_i^P\right|\hat{\sigma}_i/\sigma_0 \quad \text{(no summation on i)} \tag{16}$$

The above framework is fully specified for multiaxial behavior once the six input histories, $\hat{\sigma}_i$, and the coefficients, $\hat{\nu}_1$, $\hat{\nu}_2$, $\hat{\nu}_3$, are specified in terms of the plastic strains ε_i^P and the strain rates $\dot{\varepsilon}_i^P$. Two approaches, *independent hardening* and *coupled hardening*, to specify the strain dependence of $\hat{\sigma}_i$ will be described below.

Compromises in representing actual multiaxial stressing behavior are inevitable at this stage because multiaxial behavior is generally quite complex, as is well known even for conventional plastic solids. Here, following Xue and Hutchinson (2005), we propose two hardening laws for multi-axial stressing: *independent hardening* and *coupled hardening*. Both reproduce the stress-strain behavior, $\hat{\sigma}_i(\varepsilon_i^P, \dot{\varepsilon}_i^P)$, for each of the six simple stress histories when σ_i acts singly. In orthotropic axes, the constitutive model predicts identical stress-strain behavior in

tension and compression or in positive or negative shear (i.e. with a change in sign of σ_i). Thus, the choice of each of the basic histories, $\hat{\sigma}_i(\varepsilon_i^P, \dot{\varepsilon}_i^P)$, should be guided by the specific application. For example, if core crushing in one of the orthotropic directions is relevant, then $\hat{\sigma}_i(\varepsilon_i^P, \dot{\varepsilon}_i^P)$ for that direction should be based on compression data.

2.3.1 Independent hardening

The most straightforward algorithm for multi-axial stressing takes each of the six hardening functions, $\hat{\sigma}_i$, to be affected only by the magnitudes of associated plastic strain component, ε_i^P, and associated constant strain rate, $\dot{\varepsilon}_i^P$. Let

$$\dot{\eta}_i^P = \left|\dot{\varepsilon}_i^P\right| \tag{17}$$

and take each of the hardening functions as $\hat{\sigma}_i(\eta_i^P, \dot{\eta}_i^P)$. For stressing with $\sigma_i > 0$ as the only component, this reduces to the input function for each given associated strain rate,$\dot{\varepsilon}_i$. This is *independent hardening* in the sense that the intercept of the yield surface with each axis in stress space is only affected by the component of plastic strain conjugate to that stress component. Plastic straining in one direction does not affect the yield strength in the other directions according to this prescription. The strain dependence of the $\hat{\nu}_{ij}^P$ must also be specified. For many applications involving crushing and shear deformations of highly porous core materials, the choice $\hat{\nu}_i = 0$ $(i = 1, 3)$ will be expedient. Alternative prescriptions are discussed in the Appendix.

This constitutive model has common features with the independent hardening constitutive models used in codes such as LS-DYNA [LS-DYNA manual (1998)] where a "box-shaped" polyhedral yield surface in orthotropic axes is comprised of planes specified by the magnitudes of each of the stress components. Both reproduce the stress-strain behavior when the stress components act singly. However, in the present model, the yield surface retains an ellipsoidal shape with hardening or softening. Thus, the present model produces a genuine interaction among the stress components under multiaxial stressing, in much the same manner as classical plasticity models, and, for most materials, is more likely to be representative of multiaxial behavior. On the other hand, the planar yield surface models have the advantage that they can be formulated to specify distinct behavior in tension and compression simultaneously for each of the uniaxial stress components. As mentioned earlier, in the form introduced here, the ellipsoidal yield surface model only permits data input for either tensile or compressive behavior of each uniaxial stress component, but not both.

2.3.2 Coupled hardening

The *coupled hardening* algorithm ties changes in each of six hardening functions $\hat{\sigma}_i$ and the $\hat{\nu}_1$, $\hat{\nu}_2$, $\hat{\nu}_3$ to the effective plastic strain, ε_{eff}^P, defined by (5) and (10), by taking $\hat{\sigma}_i(\eta_i^P, \dot{\eta}_i^P)$ and $\hat{\nu}_i(\eta_i^P, \dot{\eta}_i^P)$ in the yield function where

$$\dot{\eta}_i^P = (\sigma_0/\hat{\sigma}_i)\dot{\varepsilon}_{eff}^P \tag{18}$$

Note that, according to (16), this recipe also reduces to $\dot{\eta}_i^P = \left|\dot{\varepsilon}_i^P\right|$ when $\sigma_i > 0$ is the only non-zero stress component. Thus, this prescription has each of the six hardening functions depending on ε_{eff}^P in such a way that the model also replicates the input stress-strain data when any of the six stress components acts singly.

For the special case when the six hardening functions change in direct proportion to one another (uniform hardening), coupled hardening reduces to the hardening assumption made in conventional isotropic hardening. For uniform hardening, only one input stress-strain curve is required to specify the hardening behavior under multiaxial stressing and the model reduces to the version proposed by Xue and Hutchinson [2004a] and is closely related to the model proposed by Zok, Rathbun, He, Ferri, Mercer, McMeeking and Evans [2004].

2.4 Orthotropic linear elasticity

In the present constitutive model, the plasticity of the material can be supplemented by orthotropic linear elasticity. In the axes of orthotropy, the elastic properties are specified by the elastic constants: Young's moduli E_1, E_2, E_3; Poisson ratios ν_{12}, ν_{13}, ν_{23}, ν_{21}, ν_{31}, ν_{32} (only three of which are independent as discussed below); and shear moduli G_4, G_5, and G_6 such that

$$\begin{aligned} \dot{\boldsymbol{\sigma}} &= \mathbf{L}(\dot{\boldsymbol{\varepsilon}} - \dot{\boldsymbol{\varepsilon}}) \\ \dot{\boldsymbol{\varepsilon}} - \dot{\boldsymbol{\varepsilon}} &= \mathbf{M}\dot{\boldsymbol{\sigma}} \end{aligned} \tag{19}$$

where $\mathbf{L}$ and $\mathbf{M}$ are the symmetric matrices of elastic moduli and compliances given by

$$\mathbf{M}=\mathbf{L}^{-1}=\begin{bmatrix} 1/E_1 & -\nu_{21}/E_2 & -\nu_{31}/E_3 \\ -\nu_{12}/E_1 & 1/E_2 & -\nu_{32}/E_3 \\ -\nu_{13}/E_1 & -\nu_{23}/E_2 & 1/E_3 \\ 0 & 0 & 0 \\ 0 & 0 & 0 \\ 0 & 0 & 0 \end{bmatrix} \begin{bmatrix} 0 & 0 & 0 \\ 0 & 0 & 0 \\ 0 & 0 & 0 \\ 1/G_4 & 0 & 0 \\ 0 & 1/G_5 & 0 \\ 0 & 0 & 1/G_6 \end{bmatrix} \tag{20}$$

Here, ν_{ij} are defined in the usual manner. Elastic symmetry requires $\nu_{ij}/E_i=\nu_{ji}/E_j$ such that only three of the ν_{ij} are independent. Additionally, positive definiteness of $\mathbf{L}$ and $\mathbf{M}$ requires

$$\begin{cases} E_1,\ E_2,\ E_3,\ G_4,\ G_5,\ G_6 > 0 \\ |\nu_{12}| < \left(E_1/E_2\right)^{1/2} \\ |\nu_{13}| < \left(E_1/E_3\right)^{1/2} \\ |\nu_{23}| < \left(E_2/E_3\right)^{1/2} \\ 1-\nu_{12}\nu_{21}-\nu_{23}\nu_{32}-\nu_{31}\nu_{13}-2\nu_{21}\nu_{32}\nu_{13} > 0 \end{cases} \tag{21}$$

In principle, equations (20) and (21) can be determined and verified from the six stress-strain histories. In particular, uniaxial stressing along each of the axes of orthotropy provides the Young's moduli and Poisson ratios, while three pure shear tests provide the shear moduli.

2.5 *Incremental relations among the stresses and strains*

The two versions of the constitutive model are fully specified. It only remains to obtain the incremental relations among the stresses and strains. Here, the incremental relations are derived and expressed in matrix/vector form. Plastic yielding at *constant strain-rate* requires $\dot{f}=\dot{\sigma}_{eff}=0$, or

$$\boldsymbol{\sigma}\mathbf{P}\dot{\boldsymbol{\sigma}}+\frac{\partial\sigma_{eff}}{\partial\varepsilon^P_{eff}}\dot{\varepsilon}^P_{eff}=0 \tag{22}$$

Using (9), (19) and (22), it is readily shown that

$$\dot{\varepsilon}^P_{eff}=\left(\frac{\boldsymbol{\sigma}\mathbf{P}\mathbf{L}\mathbf{P}\boldsymbol{\sigma}}{\sigma_{eff}}+\frac{\partial\sigma_{eff}}{\partial\varepsilon^P_{eff}}\right)^{-1}\boldsymbol{\sigma}\mathbf{P}\mathbf{L}\dot{\boldsymbol{\varepsilon}} \tag{23}$$

Equations (9), (19) and (23) provide the tangent moduli relating the stress and strain increments:

$$\dot{\boldsymbol{\sigma}}=\overline{\mathbf{L}}\dot{\boldsymbol{\varepsilon}}=\left[\mathbf{L}-\left(\boldsymbol{\sigma}\mathbf{P}\mathbf{L}\mathbf{P}\boldsymbol{\sigma}+\sigma_{eff}\frac{\partial\sigma_{eff}}{\partial\varepsilon^P_{eff}}\right)^{-1}\mathbf{L}\mathbf{P}\boldsymbol{\sigma}\boldsymbol{\sigma}\mathbf{P}\mathbf{L}\right]\dot{\boldsymbol{\varepsilon}} \tag{24}$$

Expressions for $\partial\sigma_{eff}/\partial\varepsilon^P_{eff}$ for each of the hardening laws are given in the Appendix. If $\overline{\mathbf{L}}$ is non-singular, $\dot{\boldsymbol{\varepsilon}}=\overline{\mathbf{M}}\dot{\boldsymbol{\sigma}}$ where $\overline{\mathbf{M}}=\overline{\mathbf{L}}^{-1}$.

The plastic strain-rate, $\dot{\varepsilon}^P$, has been assumed constant in deriving the above constitutive equations. As is customary in generalizing constant strain-rate data to plasticity applications were the strain-rate itself varies with respect to time, the accelerations of the plastic strains are ignored in the equations, if for no other reason that stress-strain data under varying strain rates is generally not available. Thus, the above equations are proposed as the constitutive model under general conditions of stressing and straining.

The present constitutive model has been implemented into ABAQUS/Explicit [ABAQUS Manual (2004)] through its VUMAT subroutine interface. The computational algorithm in the VUMAT code is analogous to that developed for a more restricted sub-set of constitutive models in Xue and Hutchinson [2004a].

3 Application to sandwich plates with square honeycomb cores

The second half of the paper demonstrates application of the constitutive model to investigate responses of a sandwich plate with a square honeycomb core (Fig. 1) to a quasi-static punch load and dynamic impulsive pressure loads using finite element methods. The first step in employing the constitutive law is identification of the input stress-strain data: $\hat{\sigma}_i$ and $\hat{\nu}_i$, and the elastic constants. The analyst has several options at his or her disposal for this purpose, including using experimental data, using predictions from theoretical models or using predictions from numerical simulations. In this paper, a combination

of the two latter approaches is employed. Computed simulations of the response of the square honeycomb core for the most relevant basic stress histories are used along with strength of materials estimates of the elastic constants and yield behavior. For clamped sandwich plates subject to transverse loads, the important basic stressing histories of the core are: (1) crushing normal to the sandwich faces, (2) out-of-plane

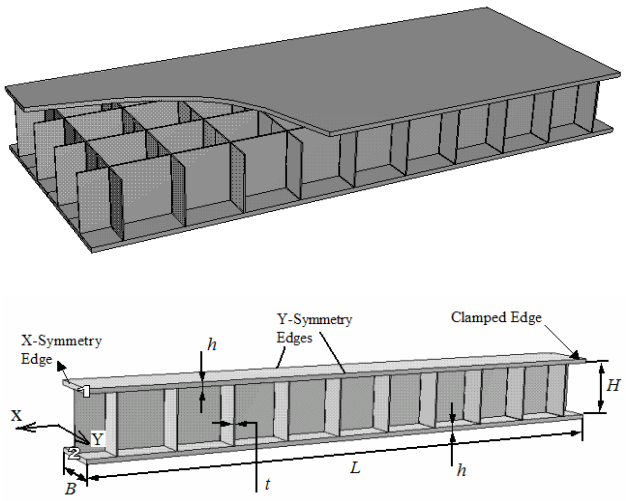

Figure 1 : Schematic diagram of square honeycomb sandwich plate configuration and corresponding computation model of sandwich panel.

shear, and (3) in-plane stretching. Each of these can contribute significantly to the overall load-deflection behavior of the plate, and thus they must be modeled with some fidelity. The core webs in the examples illustrated undergo plastic yielding either prior to buckling or nearly simultaneously with buckling. Under crushing, the square honeycomb core softens dramatically once the webs begin to buckle in the plastic range. At high crush rates, lateral inertia of the webs delays buckling, and thus dynamic effects play an important role in the constitutive response of the core. Core webs also undergo plastic buckling in out-of-plane shear, but without softening. In-plane stretching of the core is limited by tensile necking and/or fracture, but that is assumed to occur at strains larger than those considered here.

As mentioned above, another objective of this paper is to show that it is possible to use the constitutive model within a finite element formulation using only one element through the thickness of the core, motivated by the significant reduction in the number of elements required to represent a large sandwich plate structure. Any approach based on employing one element through the thickness necessarily fails to capture certain features of core response, such as wave propagation through the core or spatial details of crush development through the core. If knowledge of such details is deemed essential then the analyst probably has no recourse other than to carry out an analysis using a full three-dimensional representation of the core. However, if the primary interest is in the overall response of the plate structure, then it will be shown that the *one-element* approach based on proper calibration of present constitutive model can be accurate and computationally efficient.

3.1 Specification of the plate

Two loadings, one quasi-static and one dynamic, will be applied to the steel sandwich plate depicted in Fig. 1, which is infinitely long, of width $2L$ and clamped along the sides. Each of the loadings is uniform in the direction parallel to the infinite dimension. The honeycomb sandwich plate has core height, H, core web thickness, t, face sheet thickness, h, and web spacing B. The density of the steel comprising the faces and webs is $\rho_s = 8000 kg/m^3$. The volume fraction of the core occupied by steel can be expressed in terms of t and B as

$$\overline{\rho}_c = 2\frac{t}{B} - \left(\frac{t}{B}\right)^2 \cong 2\frac{t}{B} \tag{25}$$

and the total mass/area of the sandwich plate, $\overline{M}$, is given by

$$\overline{M} = \rho_s(2h + \overline{\rho}_c H) \tag{26}$$

The plate considered in all the numerical simulations has $L = 1m$, $h/L = 0.009$, $H/L = 0.1$, $B/L = 0.1$, $t/H = 0.01$, corresponding to $\overline{\rho}_c = 0.02$, and $\overline{M} = 160 kg/m^2$ $(\overline{M}/(\rho_s L) = 0.02)$. The core mass is 10% of the total.

The core webs and face sheets of the sandwich plate are assumed to be 304 stainless steel. A piecewise function has been fit to the true stress-log strain tensile behavior of the material giving

$$\sigma = \begin{cases} E\varepsilon & \varepsilon \le \sigma_Y/E \\ \sigma_Y \left(E\varepsilon/\sigma_Y\right)^N & \varepsilon > \sigma_Y/E \end{cases} \tag{27}$$

with Young's modulus $E = 200GPa$, Poisson's ratio $\nu = 0.3$, tensile yield strength $\sigma_Y = 205MPa$, and strain hardening exponent $N = 0.17$. Strain-rate sensitivity of the steel has not been taken into account. Classical flow theory of plasticity based on the Mises yield surface and isotropic hardening is employed to represent the face sheets in all the computations and the core webs in the three-dimensional simulations. Fracture is not considered; the steel is assumed sufficiently ductile to sustain the strains that arise.

4 Quasi-static punch loading

4.1 Identification of the constitutive inputs

Plastic deformation of the square honeycomb core is well approximated by $\hat{\nu}_i = 0$ $(i = 1,3)$, and that is adopted here. For quasi-static deformations the inputs are $\hat{\sigma}_i(\varepsilon_P)$, and, as mentioned above, the three that are important are $\hat{\sigma}_1$, $\hat{\sigma}_3$ and $\hat{\sigma}_4$. These are calculated using a three dimensional finite element representation of the unit core cell shown in Fig. 2, which is subject to periodic displacement boundary conditions consistent with the basic stress histories, as discussed in detail by Xue and Hutchinson [2004a]. Thus, to determine $\hat{\sigma}_3$ for crushing, the faces are taken as rigid and displaced in the 3-direction towards one another, with zero shear tractions and zero displacements parallel to the faces enforced at the edges of the webs in the unit cell. The average normal stresses in the three directions are computed and converted to relations between true stress and logarithmic strain. Once plastic deformation is dominant, the average stress parallel to the faces becomes small compared to $\hat{\sigma}_3$, consistent with taking the associated plastic Poisson ratios to be zero. Similar computations are made for in-plane stretching ($\hat{\sigma}_1$) and out-of-plane shear ($\hat{\sigma}_4$) as described more fully by Xue and Hutchinson [2004a]. The results, shown in Fig. 2, have been normalized by their initial values, $\hat{\sigma}_i(0)$, determined based on simple estimates from the strength of materials under the assumption that plastic yielding occurs prior to elastic buckling,

$$\begin{cases} \hat{\sigma}_1(0) = \hat{\sigma}_2(0) = \frac{1}{2}\overline{\rho}_c\sigma_Y \\ \hat{\sigma}_3(0) = \frac{2}{\sqrt{3}}\overline{\rho}_c\sigma_Y \\ \hat{\sigma}_4(0) = \hat{\sigma}_5(0) = \frac{1}{2}\overline{\rho}_c\tau_Y \end{cases} \tag{28}$$

where $\tau_Y = \sigma_Y/\sqrt{3}$. The factor $(2/\sqrt{3})$ for web materials having a Mises yield surface reflects the constraint of the faces such that the webs undergo plane strain compression under crushing.

The initial geometry of the three-dimensional unit cell is imperfection-free. Buckling is triggered by very small numerical "imperfections" such as round off error or meshing asymmetry. Particularly in the case of the dynamic simulations, imperfections can reduce the strength of the core [Xue and Hutchinson (2005)], thus the results generated for the input functions in this study apply to near-perfect cores. For a specific construction, the method used to generate the input functions should account for representative imperfections.

The webs of the core with $\overline{\rho}_c = 0.02$ buckle elastically at a slightly lower overall stress than $\hat{\sigma}_3(0)$ in (28), although this is not evident in Fig. 2 because the strain range governed by elastic buckling is a small fraction of ε_Y. As soon as plastic deformation begins, the crushing strength $\hat{\sigma}_3(\varepsilon_3^P)$ falls sharply. In out-of-plane shear, $\hat{\sigma}_4(\varepsilon_3^P)$, plastic yielding under rising stress occurs prior to buckling. Once buckling occurs, the stress remains almost constant. The curve for in-plane stretching reflects the tensile stress-strain behavior of the web oriented parallel to the direction of stressing; the curve is terminated at a strain below the necking strain for the web. The overall elastic moduli associated with each of the loading histories are also taken as strength of materials estimates:

$$\begin{cases} E_1 = E_2 = \frac{1}{2}\overline{\rho}_c E \\ E_3 = \overline{\rho}_c E_s \\ G_4 = G_5 = \frac{1}{2}\overline{\rho}_c G \end{cases} \tag{29}$$

where $G = E/(2(1+\nu))$.

To complete the inputs for quasi-static problems, one needs to specify the in-plane shear response $\hat{\sigma}_6(\varepsilon_6^P)$ and elastic shear modulus G_6. These are exceeding low and essentially irrelevant to performance of the square honeycomb core plate because the face sheets supply essentially all the in-plane shear strength and stiffness. They are taken as

$$\hat{\sigma}_6(\varepsilon_6^P) = \frac{1}{200}\overline{\rho}_c\tau_Y, \quad \text{and} \quad G_6 = \frac{1}{2000}\overline{\rho}_c G \tag{30}$$

To illustrate interaction among the stresses under multiaxial stressing, initial yield (defined for present purposes as the onset of significant nonlinearity) have been calculated using the three-dimensional cell for combinations

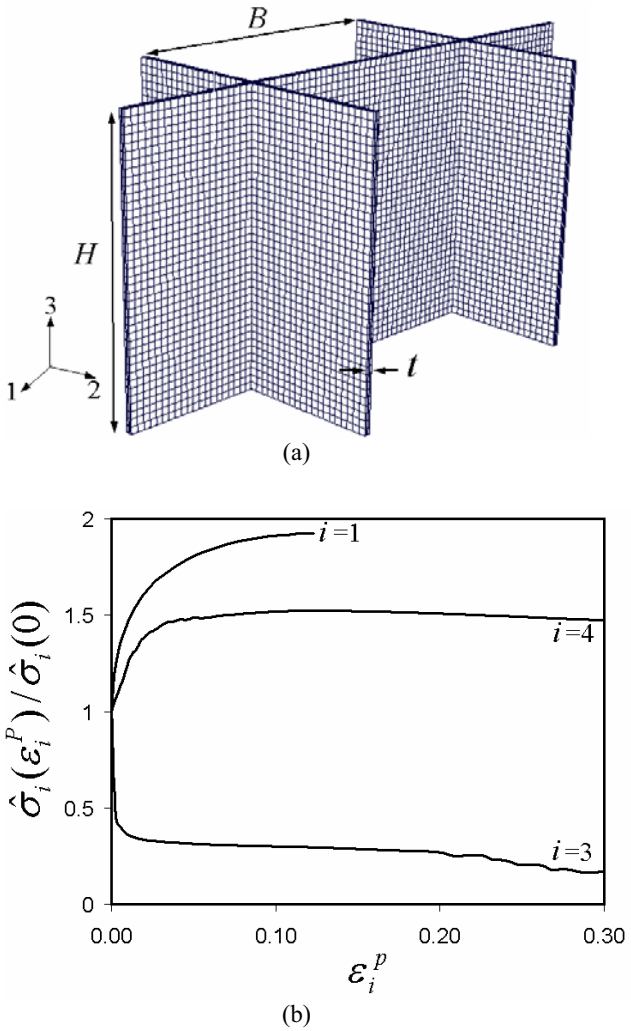

Figure 2 : Normalized true stress-plastic strain relationships for three basic histories of the square honeycomb core: $H/B = 1$ and $t/B = 0.01$ corresponding to $\overline{\rho}_c = 0.02$ with material properties stated in the text. The true stresses are normalized by the initial yield stresses (28).

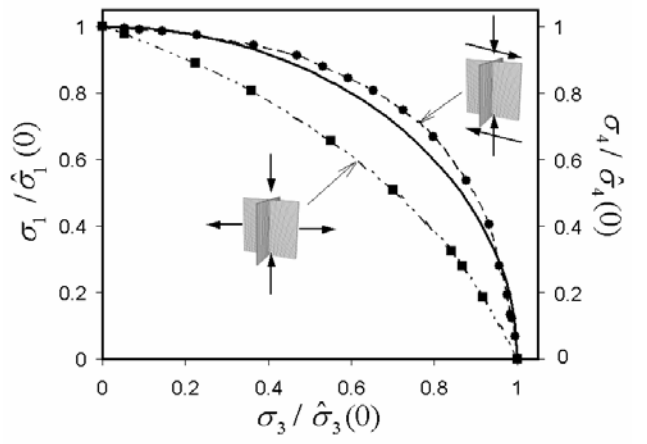

Figure 3 : The initial yield surface of the square honeycomb core under two combined loadings: (I) combined core crushing and out-of-plane shear and (II) combined core crushing and in-plane tension. The *solid line* corresponds to the ellipsoidal surface invoked in the constitutive model with $\hat{\nu}_1 = \hat{\nu}_2 = \hat{\nu}_3 = 0$. The square honeycomb core has the same geometrical parameters as that in Fig. 2.

(σ_1,σ_3) and (σ_3,σ_4) and compared in Fig. 3 with results for initial yield predicted from the continuum yield surface (3). The cell results are close to what one would obtain directly from the Mises yield surface in plane stress without accounting for any non-uniformity of stress in the webs. Yield for the combination (σ_3,σ_4) predicted by the continuum yield surface accurately captures the interaction, while that for (σ_1,σ_3) underestimates the interaction. For initial yield, it is evident that a polygonal yield surface specified by planes perpendicular to the individual stress axes would significantly underestimate the interaction among the stress components.

Like the plate, the rigid punch in Fig. 4a is infinite in the direction perpendicular to the cross-section shown. It's half-width and edge radius are specified by $a_{punch}/L = 0.3$ and $R_{punch}/a_{punch} = 0.334$. The problem employing the constitutive model for the core satisfies plane strain conditions, rendering the problem two-dimensional. The inputs, $\hat{\sigma}_1$, $\hat{\sigma}_3$ and $\hat{\sigma}_4$, in Fig. 2 have been transferred directly into the code, while the other inputs are entered as analytical expressions as given above. Alternatively, functions could have been fit to the responses in Fig. 2 and then entered as analytical descriptions.

To assess the accuracy of the calculations based on the core constitutive model, a fully three-dimensional computation of the punch loaded plate with detailed meshing of the core members has been carried out using ABAQUS. It exploits the periodicity of the plate in its long direction employing the cellular unit of the plate shown in Fig. 1. As in the computation of the basic histories, the core webs have no initial imperfections. Details of the finite element modeling with full meshing of the core members have been described in Xue and Hutchinson [2004b]. In both sets of calculations, the faces are

modeled by the classical plasticity with Mises yield criterion and isotropic hardening, as are the core members in the full three-dimensional simulations. The punch is modeled by a rigid element, and it is assumed that contact between the punch and the plate is frictionless. In the computations based on the core constitutive model, one element is taken through the core, 4 elements through each face sheet, and 200 elements along the half-width of the plate in the core and the faces.

The comparisons presented in Fig. 4b-d will now be described in detail. To highlight the role of the constitutive law inputs, calculations for four sets of inputs have been carried out:

A) All six input functions, $\hat{\sigma}_i$, as specified above with independent hardening.

B) All six input functions, $\hat{\sigma}_i$, as specified above with coupled hardening.

C) With initial yield stresses, $\hat{\sigma}_i(0)$, as specified above: $\hat{\sigma}_i(\eta_i^P) = \hat{\sigma}_i(0)\left(\hat{\sigma}_3(\eta_3^P)/\hat{\sigma}_3(0)\right)$ with coupled hardening. This is uniform hardening scaled by the initial yield stresses with all components hardening or softening as specified by the crushing response, $\hat{\sigma}_3(\eta_3^P)$.

D) With initial yield stresses, $\hat{\sigma}_i(0)$, as specified above: $\hat{\sigma}_i(\eta_i^P) = \hat{\sigma}_i(0)\left(\hat{\sigma}_4(\eta_3^P)/\hat{\sigma}_4(0)\right)$ with coupled hardening. This is uniform hardening scaled with the initial yield stresses with all components hardening or softening as specified by the shear response, $\hat{\sigma}_4(\eta_3^P)$.

4.2 Comparison of simulations under punch load

The load-center deflection response is shown in Fig. 4b, where the load per unit length, P, is normalized by the limit load per unit length, $P_c = 4\sigma_Y hH/L$, for a perfectly plastic sandwich plate with a central load (based only on contributions from the faces). The compressive crushing strain of the core (change in distance between the faces divided by H) under the punch, $\overline{\varepsilon}_c$, is plotted in Fig. 4c, and the deformed shape of the plate at $\delta_{Punch}/L = 0.25$ is displayed in Fig. 4d.

The dimensions of the sandwich plate and its material properties are such that the sequence of nonlinear behavior as predicted by the three-dimensional simulation is as follows. Core yielding in shear is the first occurrence of nonlinear behavior at $\delta_{Punch}/L \cong 0.01$. Yielding of the faces due to overall bending sets in at $\delta_{Punch}/L \cong 0.05$, followed shortly thereafter by nonlinear stretching of both faces. Finally, at $\delta_{Punch}/L \approx 0.18$, core crushing occurs due to buckling and yielding of the core webs beneath the punch. The transitions in this sequence are mirrored in the plots for the three-dimensional simulation in Fig. 4. Two views of the deformed plate at $\delta_{Punch}/L = 0.25$ from this simulation are shown in Fig. 4d.

Predictions based on each of the four sets of inputs, A-D, to the constitutive model are also shown in Fig. 4. The two inputs using all six basic stress-strain curves (A and B) rather accurately reproduce the entire load-deflection curve, the crushing strain and the final deformed shape. Moreover, there is little difference between predictions based on independent hardening (A) and coupled hardening (B). Uniform "hardening" based on inputting the crushing stress-strain curve (C) severely underestimates the early strength of the sandwich plate because of the unrealistic representation of the shear behavior. This representation even leads to less crushing in later stages (Fig. 4d). When uniform hardening based on the shear curve input (D) is used, the overall behavior is well replicated for deflections up to about $\delta_{Punch}/L = 0.18$, when substantial crushing begins. The unrealistic hardening behavior in crushing represented by D, as opposed to softening, suppresses nearly all core crushing, as is evident in Fig. 4d.

The example illustrates that accurate predictions of punch loading of the sandwich plate using a continuum model of the core require realistic representations of the crushing and shear behavior of the core. The constitutive model enables these inputs. Significant in-plane stretching of the core also occurs, but its contribution to the overall load-deflection behavior is relatively small compared to the contribution of the face sheets since the web mass parallel to the stretch direction constitutes only 5% of the total mass.

5 Distributed impulsive load

5.1 Identification of constitutive inputs

The sandwich plate analyzed in this section is precisely same as that specified in Section 3.1. Three-dimensional cell model computations have been carried out to generate the rate-dependent constitutive inputs in crushing, $\hat{\sigma}_3(\varepsilon_3^P, \dot{\varepsilon}_3^P)$, and out-of-plane shear, $\hat{\sigma}_4(\varepsilon_4^P, \dot{\varepsilon}_4^P)$. As discussed by Xue and Hutchinson [2005], there are three distinct effects contributing to the response of a square honeycomb core under dynamic loading: i) inertial re-

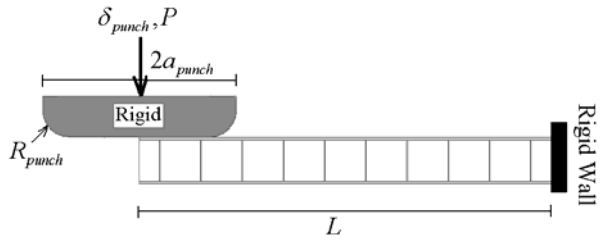

(a)

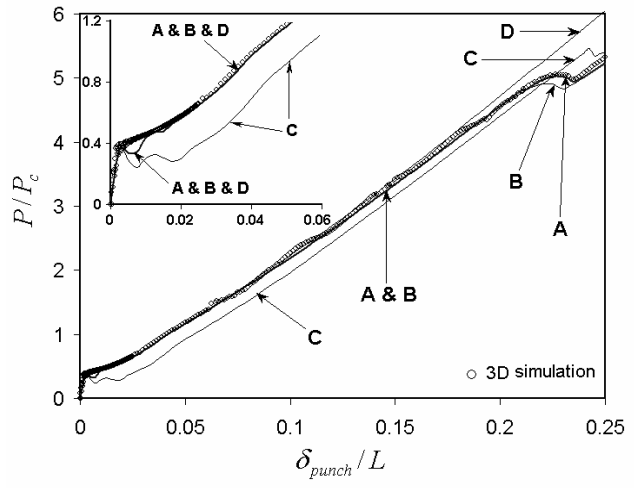

(b)

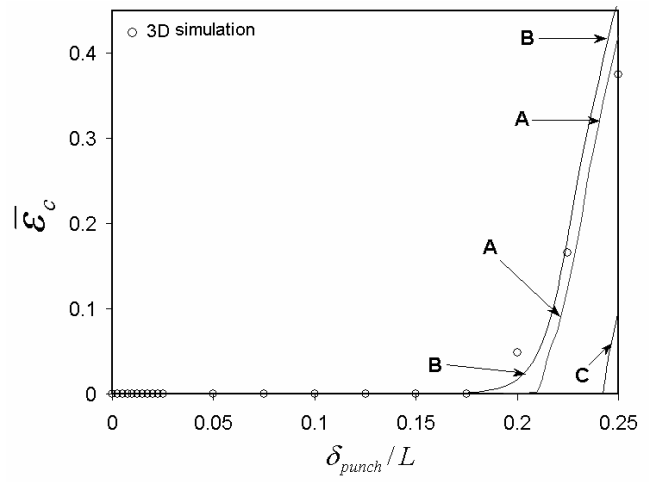

(c)

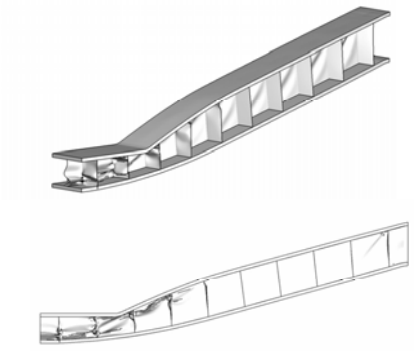

3D simulation (two views)

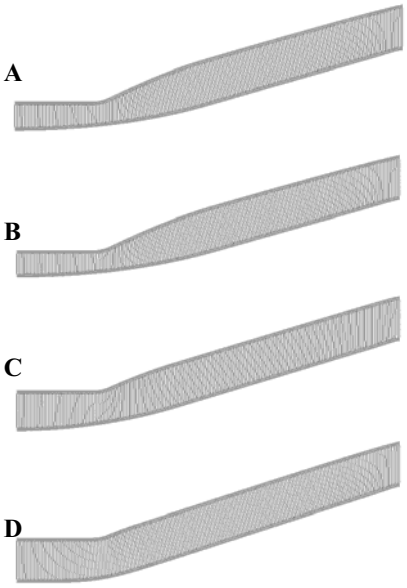

(d)

Figure 4 : Comparison of the results of three dimensional finite element analysis of the clamped square honeycomb core sandwich plate subject to quasi-static punch loading with the results computed with plane-strain continuum core model. Four sets of constitutive inputs, A-D, specified in Section 4.1, have been considered. (a) Schematic diagram of square honeycomb core sandwich plate subject to punch loading. (b) The relation between P/P_c and δ_{Punch}/L. (c) The average compressive strain of the core at its middle section. (d) The deformed configuration at $\delta_{Punch}/L = 0.25$ for each simulation.

sistance manifest as plastic wave propagation, ii) inertial stabilization of webs against buckling, and iii) material strain-rate dependence. Of the three effects, material rate-dependence is the most straightforward to incorporate into the constitutive inputs, and, to reduce the number of effects being considered, it has not been included in this paper.

The identification process for dynamic problems differs for approaches that use one element through the core thickness from those employing many elements through the thickness. In the latter, the core mass is distributed throughout the thickness and some aspects of plastic wave propagation through the thickness are simulated in the finite element calculation. The process of identifying the inputs for such approaches was illustrated by Xue and Hutchinson [2005]. In the present approach with only one element through the thickness, core mass is allocated to the faces and effects associated with plastic wave propagation are not directly computed. Instead, they must be incorporated via the inputs. An effective way to do this is described next which does not "double account" for inertial effects associated with overall motion of the core's center of mass.

In crushing, at $t = 0$ a uniform velocity, -V_0, is applied abruptly to upper face of the cell with velocity, V_0, applied to the lower face such that the overall crushing rate is $\dot{\bar{\varepsilon}} = 2V_0/H$. Assuming symmetric deformation with respect to the core mid-plane, the center of mass of the core remains motionless. Otherwise, boundary conditions for the cell are the same as those used in Section 4. The average compressive stress exerted by the core on the face sheets is identified with $\hat{\sigma}_3$. Histories of $\hat{\sigma}_3$ as a function of ε_3^P are presented in Fig. 5a for various overall crushing rates over the range of rates expected to be relevant for impulsive loadings. At high rates, the elevation of the core crushing strength is very large, considerably larger than the elevation that would be due to material rate effects. The elevation results from both inertia resistance, which increases the initial levels of $\hat{\sigma}_3$, and retardation of web buckling, which postpones the onset of softening. For example, at $\dot{\bar{\varepsilon}} = 500s^{-1}$ buckling is delayed until $\varepsilon_3^P \cong 0.1$ whereupon the core strength begins to fall abruptly with increasing crushing strain.

Analogous behavior is seen in Fig. 5b for the out-of-plane shear strength $\hat{\sigma}_4$ as computed from the cell model. In this case, equal and opposite uniform velocities, V_0, tangent to the faces are imposed on the three-dimensional

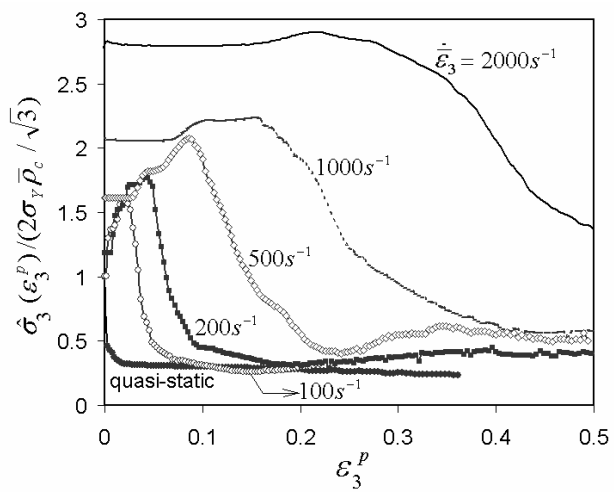

(a)

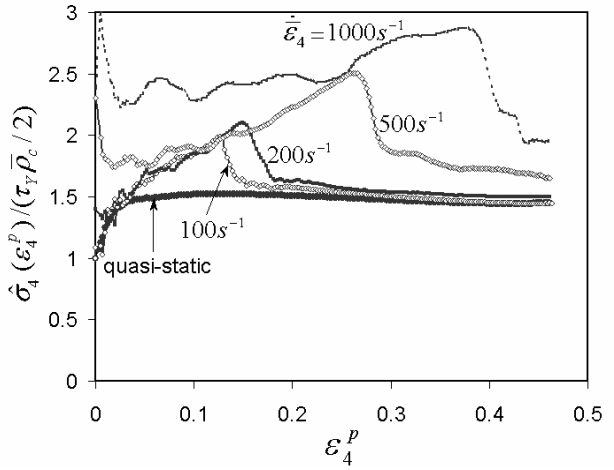

(b)

Figure 5 : The effect of overall strain rate on the normalized true stress-plastic strain relation of the square honeycomb core under (a) core crushing (b) out-of-plane shear as computed using the three dimensional cell model. The square honeycomb core has the same geometrical parameters as Fig. 2.

cell such that the overall strain rate is $\dot{\bar{\varepsilon}}_4 = 2V_0/H$. The substantial delay in shear buckling of the webs at high strain rates permits the stresses exerted on the faces to rise well above the quasi-static buckling stress. It will be seen, however, the rate-dependence in shear is not nearly as important in sandwich plate behavior as that in crushing because the strains and strain-rates experienced by the core in shear are not nearly as large as those

in crushing and because shear softening does not occur under quasi-static conditions. Under in-plane stretching, the main rate effect would be material rate-dependence, which is not accounted for here, but the effect is relatively small in any case because the stretching strain rates generally do not exceed $100s^{-1}$ and the contribution of the core to the stretching strength of the sandwich is small.

Thus, except for $\hat{\sigma}_3(\varepsilon_3^P, \dot{\varepsilon}_3^P)$ and $\hat{\sigma}_4(\varepsilon_4^P, \dot{\varepsilon}_4^P)$, the quasi-static inputs specified in the previous section will be used, along with $\hat{v}_i = 0\ (i = 1, 3)$. In the computations for the impulsively loaded plate which follow, $\hat{\sigma}_3(\varepsilon_3^P, \dot{\varepsilon}_3^P)$and $\hat{\sigma}_4(\varepsilon_4^P, \dot{\varepsilon}_4^P)$ were input into ABAQUS directly as the numerical data sets that generated the curves in Fig. 5 using interpolation over the strains and strain rates in the code. Alternatively, one could fit analytical functions to the data plotted in Fig. 5, and then input those functions [Rabczuk, Kim, Samaniego and Belytschko (2004); Xue and Hutchinson (2005)].

5.2 *Comparison of simulations under distributed impulsive load*

For $t \geq 0$, a pressure $p = p_0 e^{-t/t_0}$ is applied uniformly over the upper face sheet of the sandwich plate. The decay time of the pressure pulse is set at $t_0 = 10^{-4}s$, which is roughly 1/5 of the period in which the core undergoes dynamic crushing and about 1/50 of the time required for the plate to come to rest. Thus, the loading is nearly equivalent to an initial momentum impulse/area given by

$$I = \int_0^\infty p dt = p_0 t_0 \tag{31}$$

As in the case with the punch loading, one element was taken through the thickness of the core with meshing details similar to those described in the previous section. The mass of the core was partitioned equally to the nodes on the top and bottom face sheets. Thus, instead of being uniformly distributed throughout the core, the mass of the core is lumped at the faces. As already emphasized, plastic wave propagation through the core is not simulated, but some of its important influences have been incorporated in the constitutive inputs as rate effects. Inertial effects associated with motion of the core's center of mass are simulated. If an instantaneously applied momentum impulse is applied to one face sheet, due regard must be taken for the extra core mass attached to that face sheet in assigning the initial velocity.

Computations were carried out at different levels of dynamic loading as measured by the normalized impulse $I \Big/ \left(\overline{M}\sqrt{\sigma_Y/\rho_s}\right)$ where I is defined by (31). Comparisons of several aspects of the overall response of the sandwich plate have been made between a full dynamic three-dimensional finite element simulation [Xue and Hutchinson (2004b)] and the two-dimensional plane strain analysis based on the present continuum constitutive model. These are presented in Figs. 6-8, and will be discussed in detail below.

The previous section illustrated the importance of having correct characterization of the core behavior in crushing and shearing, at the same time indicating that there is little difference between predictions based on independent hardening and coupled hardening for this plate. In this study independent hardening will be invoked, but it has been verified for a few cases that coupled hardening gives similar predictions. However, to bring out the aspects of the core response that are most important to the overall response, we have conducted plane strain simulations with three sets of inputs:

E) The six $\hat{\sigma}_i$ described above, with $\hat{\sigma}_3$ and $\hat{\sigma}_4$ as rate-dependent.

F) The six $\hat{\sigma}_i$ described above, with $\hat{\sigma}_3$ as rate-dependent and $\hat{\sigma}_4$ as quasi-static.

G) The six $\hat{\sigma}_i$ described above, with $\hat{\sigma}_3$ and $\hat{\sigma}_4$ as quasi-static.

By contrasting F and G with E, the effects of the two rate-dependent inputs will be highlighted; the quasi-static limits of $\hat{\sigma}_3$ and $\hat{\sigma}_4$ are those used in the punch study (Fig. 5).

Fig. 6a presents the normalized maximum deflection of the top and bottom face sheets, $\delta_{\max}/L$, as a function of the dimensionless impulse. Fig. 6b presents the crushing strain in the center of the plate in the final deformed state, and Fig. 6c compares the final deformed state predicted by the three-dimensional calculation with that based on F. It is clear from Fig. 6 that the numerical results using the continuum constitutive model with either E or F capture the major features of the overall sandwich plate response with reasonable fidelity and predict the overall deflection accurately. In other words, in this application, the rate-dependence in shear (compare E and F) is not significant. This is not unexpected because both the out-of-plane shear strain and its rate are not large. By contrast, the rate dependence of crushing (compare E and

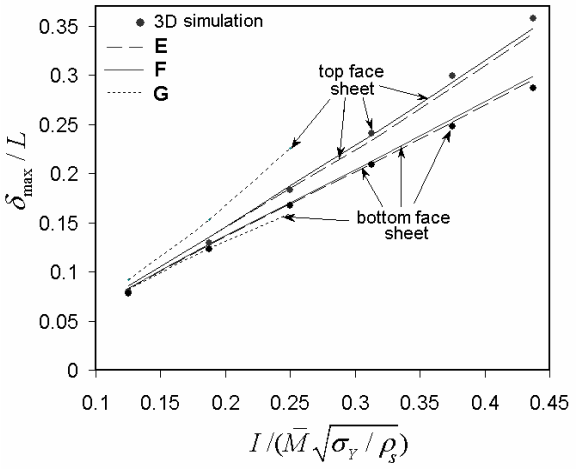

(a)

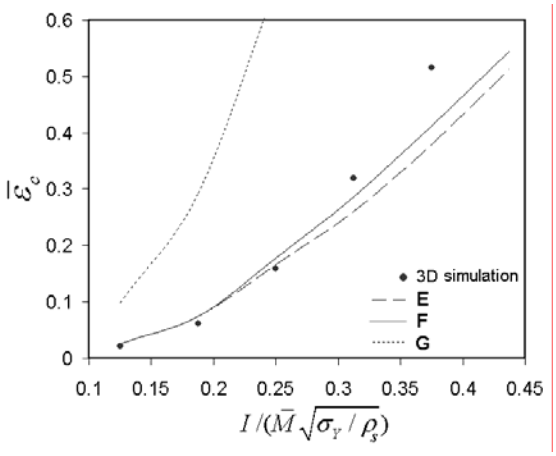

(b)

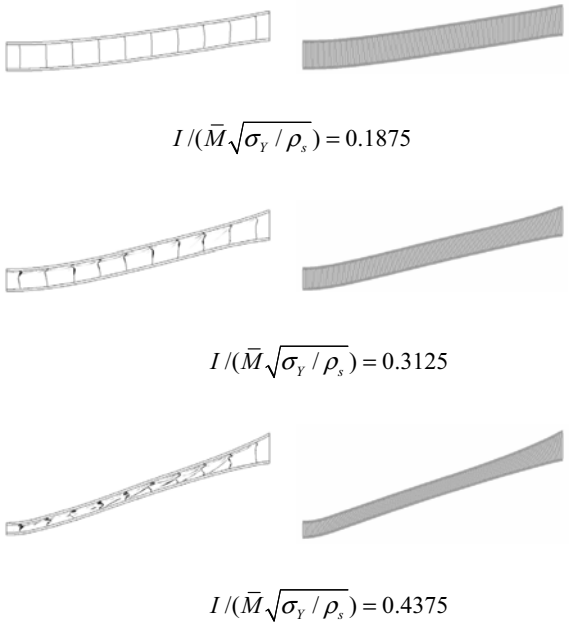

(c)

Figure 6 : Comparison of the results of three dimensional finite element simulations of the clamped square honeycomb core sandwich plate with the results of plane-strain continuum core model for uniformly distributed pressure loading $p = p_0 e^{-t/t_0}$. Calculations have been made for three sets of constitutive inputs, E, F and G, to the continuum model as specified in Section 5.2. (a) Normalized maximum deflection of the top and bottom faces of sandwich plate. (b) The residual average compressive strain of the core at its middle. (c) The deformed configuration of the square honeycomb core sandwich plates at three impulse intensities: three-dimensional simulations on the left and simulations based on F on the right.

G) has a major effect on all aspects the response. At the crushing rates representative of those for large impulsive loads ($\sim 10^3 s^{-1}$ in these examples), the crushing strength of the core is substantially elevated (c.f. Fig. 5a). This results in much less crushing of the core compared to what is predicted based on quasi-static crushing behavior and much smaller deflection of the top face sheet. Crushing input based on quasi-static behavior cannot be used to model core behavior of plates under high intensity loads. The largest discrepancy between the three-dimensional results and those based on the continuum model with input E or F is the crushing strain at the highest impulses (c.f. Figs. 6b and c and Fig. 7). At the highest impulse shown, corresponding to a final crushing strain of about 0.5, the continuum approach underestimates the final crushing strain by about 15%. This can also be seen in Fig. 7 where the crushing strain at the center of the plate is plotted against non-dimensional time

$(t/(L\sqrt{\rho_s/\sigma_Y}) = 0.4$ corresponds to $t = 2.5\times10^{-3}s$ for these plates). The one-element approach accurately reproduces the time scale of the crushing process. The error in the final crushing strain is primarily due to the fact that the dimensions of the individual plates making up the core webs $(B\times H)$ are on the scale of the core thickness itself, and the core deformation pattern also has this scale. Such deformation patterns of a discrete structure cannot rigorously be described by a continuum constitutive model. Nevertheless, the examples presented reveal it is possible to capture most of the details of overall sandwich plate deformation with reasonable accuracy. In addition, use of a single element through the thickness of the core sidesteps the spurious spatial details associated with localization in the presence of softening that emerge in formulations using multiple elements through the thickness.

Fig. 8 presents the time history of plastic dissipation in each face sheet and in the core when $I\Big/\left(\overline{M}\sqrt{\sigma_Y/\rho_s}\right) = 0.25$, comparing the three-dimensional simulation with calculations based on F. In this figure, W is the work/length done by the pressure acting on the top face, which is computed directly, and each contribution to U_P is the plastic dissipation/length integrated over the respective component of the sandwich. The agreement between the two types of simulations is excellent. The final total plastic deformation is about 5% below the work done on the plate, due primarily to residual elastic deformation.

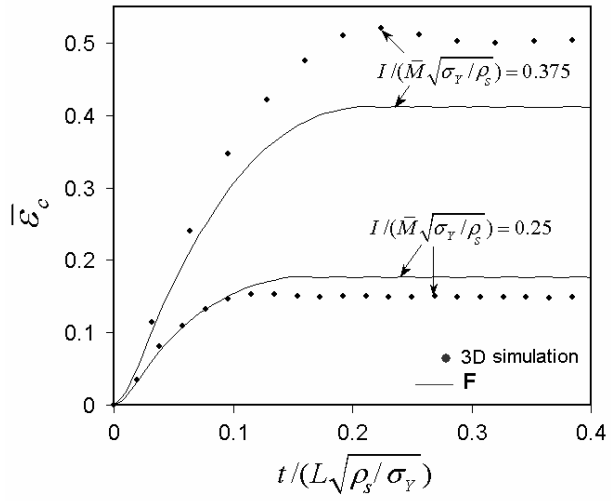

Figure 7 : The average crushing strain at the middle of the beam for the three dimensional finite element simulation and the simulation based on plane-strain continuum core model with inputs F.

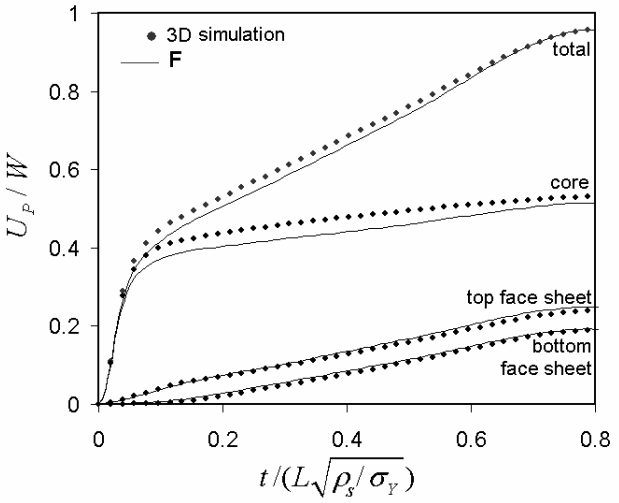

Figure 8 : The plastic energy dissipated in the sandwich plate components for the three dimensional finite element simulation and the simulation based on plane-strain continuum core model with input F $(I/(M\sqrt{\sigma_Y/\rho_s}) = 0.25)$.

6 Concluding remarks

The behavior of metal square honeycomb sandwich cores is highly nonlinear with responses that can display rapid softening in crushing or gradual hardening behavior in out-of-plane shear. Realistic representations of these very different responses are required for accurate computation of the overall response of the sandwich plate to lateral loads. The constitutive model proposed here for a plastically compressible, orthotropic material accommodates such non-uniform hardening or softening behavior. Rate-dependence of the core due to material rate-dependence or inertial effects can also be incorporated, and these can greatly affect the overall response of the plate. A process for identifying the inputs to the constitutive model has been illustrated for a specific core for an approach employing one element through the core thickness, and benchmark computations based on full meshing of the core demonstrated the validity of the approach. A user-defined constitutive module for ABAQUS Explicit has been developed based on the constitutive model.

Acknowledgement This work has been supported in

part by the ONR under grants N00014-02-1-0700 and GG10376-114934 and in part by the Division of Engineering and Applied Sciences, Harvard University. The authors are indebted to helpful suggestions from T. Belytschko, A.G. Evans and N. A. Fleck.

References

ABAQUS, Inc. *(2004): ABAQUS User's Manual, Version 6.5.*

Cote, F.; Deshpande, V. S.; Fleck, N. A.; Evans, A. G. (2004): The out-of-plane compressive behavior of metallic honeycombs. *Materials Science and Engineering A*, vol. 380, pp. 272-280.

Deshpande, V. S.; Fleck, N. A. (2000): Isotropic constitutive models for metallic foams. *J. Mech. Phys. Solids*, vol. 48, pp. 1253-1283.

Deshpande, V. S.; Fleck, N. A.; Ashby, M. F. (2001): Effective properties of the octet-truss lattice material. *J. Mech. Phys. Solids*, vol. 49, pp. 1747-1769.

Dharmasena, K. P.; Xue, Z; Wadley, H. N. G.; Hutchinson, J. W. (2005): Mechanical response of metallic honeycomb sandwich panel structures to high intensity dynamic loading, International Journal of Impact Engineering, Submitted.

Hanssen, A. G.; Langseth, M.; Hopperstad, O. S. (2002) Crush behavior of foam-based components: validation of numerical simulations. *Advanced Engng. Mater.*, vol. 4, pp. 771-776.

Hill R. (1947): A theory of the yielding and plastic flow of anisotropic materials. *Proceedings of Royal Society*, vol. A193, pp. 281-297.

Hill, R. (1950): *The mathematical theory of plasticity.* Oxford University Press, Oxford, UK.

Livermore Software Technology Corporation (1998): *LS-DYNA theoretical manual.*

Mohr, D.; Doyoyo, M. (2004): Large plastic deformation of metallic honeycomb: orthotropic rate-independent constitutive model. *Int. J. Solids Structures*, vol. 41, pp. 4435-4456.

Oller, S.; Car, E.; Lubliner, J. (2003): Definition of a general implicit orthotropic yield criterion. *Computer Methods in Applied Mechanics and Engineering*, vol. 192, pp. 895-912.

Qiu, X.; Deshpande, V. S.; Fleck, N. A. (2003): Finite element analysis of the dynamic response of clamped sandwich beams subject to shock loading. *European Journal of Mechanics A – Solids*, vol. 22, pp. 801-184.

Rabczuk, T.; Kim, J. Y.; Samaniego, E.; Belytschko, T. (2004): Homogenization of sandwich structures. *Int. J. Numer. Meth. Engng.*, vol. 61, pp. 1009-1027.

Rathbun, H. J.; Radford, D. D.; Xue, Z.; He, M. Y.; Yang, J.; Deshpande, V.; Fleck, N. A.; Hutchinson, J. W.; Zok, F. W.; Evans, A. G. (2005): Performance of metallic honeycomb-core sandwich beams under shock loading. *International Journal of Solids and Structures*, in press.

Xue, Z.; Hutchinson, J. W. (2003): Preliminary assessment of sandwich plates subject to blast loads. *Int. J. Mech. Sci.*, vol. 45, pp. 687-705.

Xue, Z.; Hutchinson, J. W. (2004a): Constitutive model for quasi-static deformation of metallic sandwich cores. *International Journal for Numerical Methods in Engineering,* vol. 61, pp. 2205-2238.

Xue, Z.; Hutchinson J. W. (2004b): A comparative study of impulse-resistant metallic sandwich plates. *Int. J. Impact Engng.*, vol. 30, pp. 1283-1305.

Xue, Z.; Hutchinson, J. W. (2005): Crush dynamics of square honeycomb sandwich cores. *International Journal for Numerical Methods in Engineering*, in press.

Zok, F. W.; Rathbun, H.; He, M.; Ferri, E.; Mercer, C.; McMeeking, R. M.; Evans, A. G. (2005): Structural performance of metallic sandwich panels with square honeycomb cores. *Philosophical Magazine*, vol. 85, pp. 3207-3234.

Appendix A: Appendix

In order to specify $\frac{\partial \sigma_{eff}}{\partial \varepsilon^P_{eff}}$ in equations (22-24) for *independent hardening* and *coupled hardening*, the following three independent plastic Poisson ratios, $\hat{\nu}^P_{12}\left(\varepsilon^P_1\right)$, $\hat{\nu}^P_{13}\left(\varepsilon^P_1\right)$ and $\hat{\nu}^P_{23}\left(\varepsilon^P_2\right)$, will be used in (11) to determine the other three ratios and the three $\hat{\nu}^P_i$. (The expressions below could be based on any other set of three independent plastic Poisson ratios.) Substituting (11) into (3), one obtains

$$\left(\frac{\sigma_{eff}}{\sigma_0}\right)^2 = \left(\frac{\sigma_1}{\hat{\sigma}_1}\right)^2 + \left(\frac{\sigma_2}{\hat{\sigma}_2}\right)^2 + \left(\frac{\sigma_3}{\hat{\sigma}_3}\right)^2 + \left(\frac{\sigma_4}{\hat{\sigma}_4}\right)^2 + \left(\frac{\sigma_5}{\hat{\sigma}_5}\right)^2 + \left(\frac{\sigma_6}{\hat{\sigma}_6}\right)^2 - 2\hat{\nu}_{12}^P\left(\frac{\sigma_1\sigma_2}{\hat{\sigma}_1^2}\right) - 2\hat{\nu}_{13}^P\left(\frac{\sigma_1\sigma_3}{\hat{\sigma}_1^2}\right) - 2\hat{\nu}_{23}^P\left(\frac{\sigma_2\sigma_3}{\hat{\sigma}_2^2}\right) \tag{32}$$

Then, for *independent hardening*, a lengthy derivation gives according (9), (17) and (32),

$$\frac{\partial\sigma_{eff}}{\partial\varepsilon_{eff}^P} = -\frac{\sigma_0^2}{\sigma_{eff}^2}\mathbf{qP}|\sigma| \tag{33}$$

where

$$\mathbf{q} = \begin{bmatrix} \frac{\sigma_1}{\hat{\sigma}_1^3}\left(\sigma_1 - 2\hat{\nu}_{12}^P\sigma_2 - 2\hat{\nu}_{13}^P\sigma_3\right)\frac{\partial\hat{\sigma}_1}{\partial\eta_1^P} + \frac{\sigma_1\sigma_2}{\hat{\sigma}_1^2}\frac{\partial\hat{\nu}_{12}^P}{\partial\eta_1^P} + \frac{\sigma_1\sigma_3}{\hat{\sigma}_1^2}\frac{\partial\hat{\nu}_{13}^P}{\partial\eta_1^P} \\ \frac{\sigma_2}{\hat{\sigma}_2^3}\left(\sigma_2 - 2\hat{\nu}_{23}^P\sigma_3\right)\frac{\partial\hat{\sigma}_2}{\partial\eta_2^P} + \frac{\sigma_2\sigma_3}{\hat{\sigma}_2^2}\frac{\partial\hat{\nu}_{23}^P}{\partial\eta_2^P} \\ \frac{\sigma_3^2}{\hat{\sigma}_3^3}\frac{\partial\hat{\sigma}_3}{\partial\eta_3^P} \\ \frac{\sigma_4^2}{\hat{\sigma}_4^3}\frac{\partial\hat{\sigma}_4}{\partial\eta_4^P} \\ \frac{\sigma_5^2}{\hat{\sigma}_5^3}\frac{\partial\hat{\sigma}_5}{\partial\eta_5^P} \\ \frac{\sigma_6^2}{\hat{\sigma}_6^3}\frac{\partial\hat{\sigma}_6}{\partial\eta_6^P} \end{bmatrix} \tag{34}$$

Similarly, for *coupled hardening*, according to (9), (18) and (32),

$$\frac{\partial\sigma_{eff}}{\partial\varepsilon_{eff}^P} = -\frac{\sigma_0^3}{\sigma_{eff}}\left[\frac{\sigma_1}{\hat{\sigma}_1^4}\left(\sigma_1 - 2\hat{\nu}_{12}^P\sigma_2 - 2\hat{\nu}_{13}^P\sigma_3\right)\frac{\partial\hat{\sigma}_1}{\partial\eta_1^P} + \frac{\sigma_2}{\hat{\sigma}_2^4}\left(\sigma_2 - 2\hat{\nu}_{23}^P\sigma_3\right)\frac{\partial\hat{\sigma}_2}{\partial\eta_2^P} + \frac{\sigma_3^2}{\hat{\sigma}_3^4}\frac{\partial\hat{\sigma}_3}{\partial\eta_3^P} + \frac{\sigma_4^2}{\hat{\sigma}_4^4}\frac{\partial\hat{\sigma}_4}{\partial\eta_4^P} + \frac{\sigma_5^2}{\hat{\sigma}_5^4}\frac{\partial\hat{\sigma}_5}{\partial\eta_5^P} + \frac{\sigma_6^2}{\hat{\sigma}_6^4}\frac{\partial\hat{\sigma}_6}{\partial\eta_6^P} + \frac{\sigma_1\sigma_2}{\hat{\sigma}_1^3}\frac{\partial\hat{\nu}_{12}^P}{\partial\eta_1^P} + \frac{\sigma_1\sigma_3}{\hat{\sigma}_1^3}\frac{\partial\hat{\nu}_{13}^P}{\partial\eta_1^P} + \frac{\sigma_2\sigma_3}{\hat{\sigma}_2^3}\frac{\partial\hat{\nu}_{23}^P}{\partial\eta_2^P}\right] \tag{35}$$